MnO_x loaded mesoporous silica for the catalytic oxidation of formaldehyde. Effect of the melt infiltration conditions on the activity – stability behavior

Guillaume Rochard,[a] Carmen Ciotonea,[a] Adrian Ungureanu,*[b] Jean-Marc Giraudon,[a] Sébastien Royer,[a] Jean-François Lamonier*[a]

Abstract: Conventional melt infiltration (over calcined SBA-15 silica support) and optimized melt infiltration (over surfactant-containing SBA-15 support) were used for the first time to prepare MnO_x nanoparticles encapsulated within the support pores. A comprehensive study on the evolution of textural, structural, and morphological characteristics of the MnO_x-silica composites as well as their redox and surface properties is reported herein by varying synthesis parameters, such as manganese loading (5, 10, 20 and 30 Mn wt. %), and post-treatment temperature (300 and 500 °C). The catalytic performances of the materials prepared in this work have been evaluated in the catalytic oxidation of formaldehyde. The results show a high performance of the SBA-15 supported manganese oxide at low- to moderate- temperatures of reaction (Temperature at 50 % of HCHO conversion into CO_2 ranging from 110° to 150°C), activity being related to Mn oxidation state (from 2.3 to 4) and MnOx phase location, confined with or without 3D spatial distribution in the support porosity or formed at the external surface of SBA-15. A high stability (60 hours), under dry air and 50% relative humidity air, is reported for MnO_x-based nanocatalysts prepared by conventional and optimized melt infiltration procedures.

Introduction

Among the volatile organic compounds (VOC), formaldehyde (HCHO) is a common molecule found in indoor environments such as offices, houses, schools and industrial plants [1]. Long-term exposures to HCHO is evidenced to be at the origin of severe respiratory system diseases and even cancer [2]. Considering the adverse effect of HCHO to human health, initiatives emerged during the last decade to limit release of HCHO in the environment, the most efficient from industrial/process point of view being the replacement of formaldehyde by other chemicals having comparable technical properties. Unfortunately, in several production domains, as in wood and furniture fields, no chemical substituents affording comparable properties with HCHO (paste, final resistance and so on) have been found. Therefore, one actual challenge is to develop efficient processes for HCHO degradation (in industry and in indoor air), in order to improve the indoor air quality in agreement with the current environmental regulations [3].

From a technical point of view, HCHO elimination can be performed by either adsorption or combustion. Regarding the adsorption process, porous materials such as activated carbons, [4] aminated silicas [5] or zeolites (e.g., faujasite) [6] are recognized as efficient adsorbents of HCOH. The highest adsorption capacities are reported for NaY zeolite, with more than 0.4 mL HCHO stored per gram of adsorbent. However, adsorption has its own limitations such as the need of a regeneration step [7] and the high-energy cost for the incineration [4b]. Owing to some obvious advantages such as: (i) a selective transformation of HCHO into harmless compounds (CO_2 and H_2O) and (ii) a lower energy consumption compared to thermal decomposition due to a lower operating temperature,[8] catalytic total oxidation appears as one of the most practical, efficient, and promising way for HCHO abatement, representing thus a key strategy to mitigate climate change and protect human health. Among the different studied catalysts [8,9] supported noble metals (Pt, Pd and Au) showed good performances at low/room temperature in the catalytic oxidation of formaldehyde [10] which can be further improved by alkaline doping [11]. It is worthy of mention that the undoped supported noble metal catalysts are generally activated at temperatures of around 50 °C to be selective to CO_2 [12]. Despite these promising results, nowadays, there is a continuous growth of interest for the catalysts containing transition metal oxide (TMO) nanoparticles (NPs) (e.g., mixed MnO_x-CeO_2 [13], MnO_x [14], TiO_2-CeO_2 [15] or Co_3O_4 [16]) due to their high catalytic capability as well as their cost-effectiveness, as compared with catalysts based on noble-metals. Nevertheless, the results showed that total oxidation reaction generally takes place at higher temperatures (>100°C) than those for noble metal supported catalysts (<50°C) [17]. Amongst these TMO nanocatalysts, those based on manganese oxides (MnO_x) are the most promising candidates, but, at the same time, they are the most challenging to design owing both to the redox properties of manganese – several oxidation states, and to the multiple oxide polymorphs found for every manganese oxidation state, each of them manifesting a distinct catalytic performance in the VOC oxidation. For instance, among the different polymorphs of MnO_2 [18], birnessite (δ-MnO_2) and cryptomelane (α-MnO_2) were found as the most active phases. Complete HCHO oxidation at temperatures of around 140 °C and even around 100 °C was reported for cryptomelane [19] and high surface area birnessite, respectively [20]. Furthermore, in the case of supported MnO_x catalysts, difficulty arises because

[a] Dr. G. Rochard, Dr. C. Ciotonea, Prof. S. Royer, Dr. J.-M. Giraudon, Prof. J.-F. Lamonier
Univ. Lille, CNRS, ENSCL, Centrale Lille, Univ. Artois, UMR 8181 - UCCS - Unité de Catalyse et Chimie du Solide, F-59000 Lille, France
E-mail: jean-francois.lamonier@univ-lille.fr

[b] Prof. A. Ungureanu
"Gheorghe Asachi" Technical University of Iasi, Faculty of Chemical Engineering and Environmental Protection, 73 D. Mangeron Bvd., 700050 Iasi, Romania.
E-mail: aungureanu@tuiasi.ro

Supporting information for this article is available on the WWW

the performances of such nanomaterials in terms of activity, selectivity and stability, generally depends on a multitude of properties that have to be simultaneously controlled: morphostructure (*e.g.*, morphology, size, dispersion, and spatial distribution of MnO_x NPs), texture (*e.g.*, specific surface area, pore volume, and pore size distribution), resistance against NPs aggregation upon thermochemical preparation steps – calcination/activation, reducibility of oxide catalysts, extent of metal oxide-support interactions, oxidation state of manganese, surface chemical composition and, presence of acid-base promoters and so forth [18], which, in turn, are influenced by the applied synthesis method and particularly, by the physico-chemical properties of the catalytic support, chemical nature and crystallographic characteristics of the active nanophase and its local environment, and thermal conditions upon calcination/activation steps. For the reasons set out, as compared with HCHO oxidation performed over bulk MnO_x, only a few catalytic studies were reported on supported MnO_x particles. MnOx NPs have been loaded on different supports such as cellulose [21], activated carbon [22] or graphene nanosheets [23]. As a very relevant example, β-MnO_2 NPs confined within the mesopores of ordered SBA-15 by classical impregnation or two-solvent methods were reported as highly efficient catalysts for the elimination of formaldehyde, achieving a complete conversion at 130 °C, an activity which is similar with that shown by tunnel and lamellar bulk manganese oxides, despite a lower Mn content for supported catalyst (*i.e.*, 15 wt.% Mn)[24]. Such good performance was ascribed to the beneficial adsorption of HCHO over the surface silanol groups of SBA-15 support, synchronized with an effective HCHO conversion into CO_2 over the MnO_2 NPs encapsulated within the pores of SBA-15. Nevertheless, the stability of these catalysts was not in detail investigated.

Motivated by these promising results, we report a strategy to obtain original catalysts for the total oxidation of formaldehyde, active and resistant to deactivation, by the confinement of small and homogeneous MnO_x NPs in the mesochannels of SBA-15 through the melt infiltration (MI) approach. Such a method was used successfully to get highly dispersed NiO, CuO, Co_3O_4, and Fe_2O_3 NPs on ordered mesoporous silica [25]. A series of catalysts obtained with different Mn loadings (5, 10, 20 and 30 wt.% Mn) and at two calcination temperatures (300 or 500 °C) was prepared through a MI procedure adapted from our recent studies on NiO-confined NPs [25c, 25e], using $Mn(NO_3)_2{\bullet}4H_2O$ as precursor taking advantage of its low cost, limited toxicity, and low melting temperature (*i.e.*, 37°C). By the MI approach proposed herein, which basically involves the time-controlled diffusion of the melted manganese nitrate precursor within the pores of either the surfactant-free, calcined SBA-15, or the as-synthesized SBA-15 occluded with Pluronic P123 surfactant, a selective localization of highly dispersed MnO_x NPs inside the mesopores can be achieved after controlled calcination and optimal Mn loading, with positive effects on the activity and/or stability of catalysts during reaction. This offers a unique opportunity to have an enhanced control over the activity-stability behavior of MnO_x-SBA-15 catalysts during HCHO oxidation. The performances of the catalysts were discussed in light of the physicochemical characterizations performed on the calcined and spent catalysts.

Table 1. Textural and structural properties of SBA-15 support and Mn containing catalysts.

Sample	Mn Load.[1] (wt.%)	S_{BET}[2] (m^2/g)	S_μ[3] (m^2/g)	V_p[4] (cm^3/g)	V_μ[5] (cm^3/g)	D_{pores}[6] (nm)	D_{cryst}[7] (nm)
SBA-15	-	782	201	1.2	0.016	6.9	-
20Mn-MIc-500	19.6	569	157	0.8	0.016	4.8-7.0	10
20Mn-MIc-300	19.5	426	125	0.6	0.016	5.4-7.1	9
SBA-15	-	786	197	1.2	0.009	7.3	-
5Mn-MIc-300	4.7	592	155	1.0	0.008	5.3-7.2	10
10Mn-MIc-300	11.4	514	129	0.8	0.003	5.4-7.3	11
30Mn-MIc-300	28.5	433	96	0.6	0.04	5.1-6.8	11
SBA-15	-	782	201	1.2	0.011	6.3	-
20Mn-IWI	-	525	158	0.7	0.022	5.2-7.0	9
20Mn-MIa-300	19.2	527	135	0.8	0.008	4.8-7.3	9

[1], Mn loading as determined by ICP-OES; [2], Specific surface area (BET method); [3], Microporous surface area (t-plot method); [4], Total pore volume; [5], Micropore volume (t-plot method); [6], Mean pore size (BJH method); [7], MnO_x average crystal domain size calculated by the Scherrer equation.

Results and Discussion

Effect of calcination temperature on the catalyst properties

Properties of 20Mn-MIc-Z (Z=300, 500) samples.

The nitrogen adsorption/desorption isotherms of parent SBA-15 and 20Mn-MIc-Z are displayed in Figure 1. All the materials present type IV isotherms with H1 hysteresis, as awaited for ordered mesoporous materials with a narrow pore size distribution of the cylindrical pores [26]. For MI-derived materials, the ordered structure is retained which indicates that the support is stable during the MI grinding process. A delay on the closure of the desorption branch of the isotherms is observed for the MnO_x-containing materials. This delay is related to the formation of so called “ink-bottle” shaped pores, formed when confined NPs are plugging the main mesopores [27] or when some constrictions form at the entrance of the pores. Indeed, as showed in Figure 2, SBA-15 exhibits a narrow pore size distribution centered at 6.9 nm whereas, after MI and calcination, a bimodal population is observed for both MI derived materials.

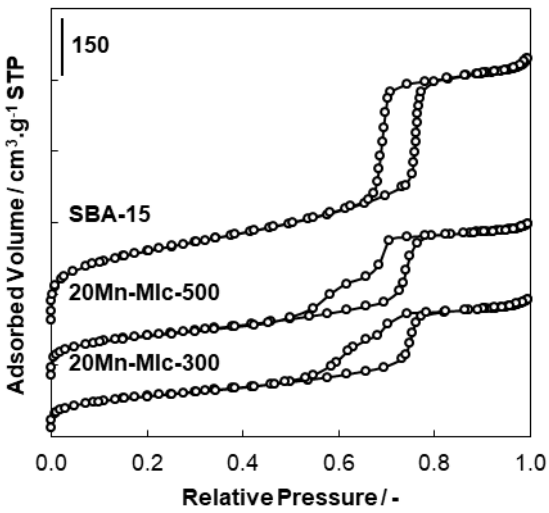

Figure 1. Adsorption/desorption isotherms (vertical shift of 150 $cm^3.g^{-1}$ each) for SBA-15 and 20Mn-MIc-Z prepared at different calcination temperatures.

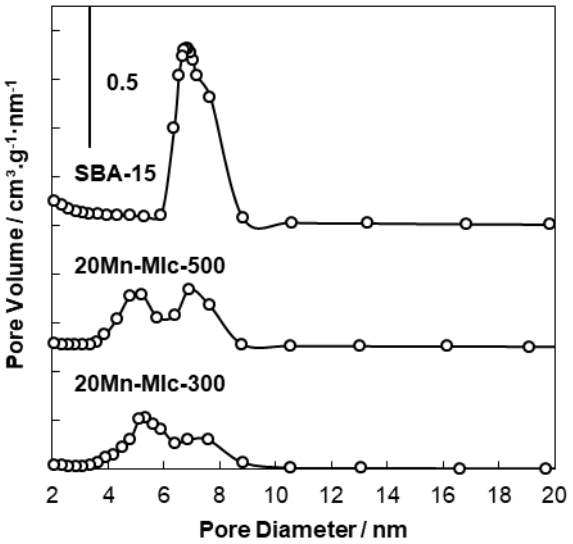

Figure 2. Pore size distribution (vertical shift of 0.5 $cm^3.g^{-1}.nm^{-1}$) for SBA-15 and 20Mn-MIc-Z prepared at different calcination temperatures.

The formation of the second porosity of ~ 5 nm diameter is then assigned to the formation of NPs filling and obstructing the main mesopores of the SBA-15 support. Most of the active phase is suggested to be located inside the mesopores, since the isotherms remains of type IV (with a long, almost horizontal, plateau associated to the N_2 capillary condensation), with no significant increase in N_2 volume adsorbed in the 0.9-1.0 P/P_0 range (a characteristic that should have been associated to the formation of external aggregates of MnO_x particles).

The textural properties were evaluated based on the adsorption/desorption isotherms and the results are summarized in Table 1. The BET surface area as well as the microporous surface area decreased for the MnO_x containing materials by comparing to the parent SBA-15 support. As previously reported by Ungureanu *et al.* [28] for Ni-Cu particles confined into SBA-15 pores, this trend can be related to the confinement of MnO_x NPs within the mesopores which can block the secondary porosity (micro- and small mesopores). The decrease is much more pronounced for 20Mn-MIc-300, suggesting that the increase in calcination temperature induces the reopening of the porosity fraction during sintering of initial dispersed MnO_x NPs. This reopening of the porosity is mostly visible on the total pore volume and total surface area, than on the micropore surface area.

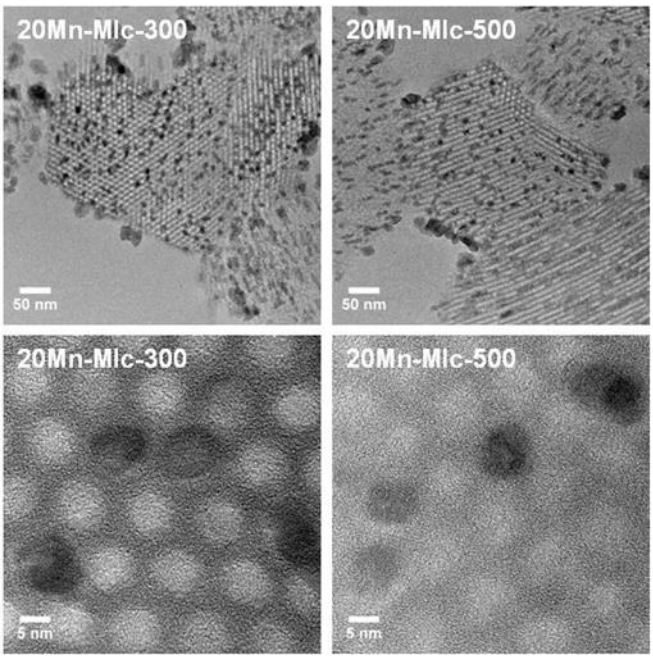

Figure 3. HR-TEM images for 20Mn-MIc-Z prepared at different calcination temperatures

The low-angle XRD patterns obtained for the SBA-15 and the 20Mn-MIc-300 samples (Figure S1) both exhibit three well-resolved peaks indexed to the (100), (110) and (200) reflections of the ordered 2D hexagonal structure of *P6mm* symmetry, as classically reported [26]. This confirms, as already observed, that the melt infiltration procedure and the further decomposition of the precursors to form the oxide MnOx phase, does not significantly alter the mesostructure long range ordering. Indeed, the decrease of the (100) reflection intensity, while the (110) and (200) reflections remains visible, is not correlated to the decrease of the pore network ordering, but is associated to the specific localization of the MnOx NPs inside the mesopores, thus reducing the electron density contrast between the pores and silica walls [28]. The wide-angle XRD patterns of the 20Mn-MIc-300 sample (Figure S2) revealed a crystallized material with three main

reflections between 35° and 65° which can be attributed to ε-MnO_2 (Akhtenskite, JCPDS 30-0820) [10c]. The broad diffraction peak at ~ 22° is attributed to the amorphous silica. [25b, 27] Heating the sample at 500 °C under air led to a more intense reflection at 2θ = 28° which can be assigned to the presence of the β-MnO_2 crystal structure (Pyrolusite, JCPDS 001-0799) [17b, 29]. Then a mixture of ε-MnO_2 and β-MnO_2 phases forms after the MI and decomposition of manganese precursor into SBA-15 porosity. The size of MnO_2 particles (9-10 nm) remains in the range of SBA-15 mesopore size [26], suggesting that crystallization took place in the confining space of the main mesopores of the silica support.

Representative TEM images are illustrated in Figure 3. As a first observation, the SBA-15 mesopores do not collapse during the MI preparation whatever the calcination temperature, confirming the N_2-physisorption results. For both materials, the MnO_2 NPs can be observed under the form of confined NPs, beside fewer external larger NPs. Particle size distribution of MnO_2 NPs represented in Figure S3 shows that the proportion of particles of size < 10 nm is about 75 % for the sample calcined at 300 °C, a comparable value being obtained for the sample calcined at 500 °C, confirming a satisfying confinement, with limited migration of manganese oxide phases outside of the mesopores when calcination temperature increases. However, a growth of the particles of size above 10 nm is observed with the increase of the calcination temperature: the average size of the external particles is ~23 nm at 500 °C compared with ~17 nm for a calcination at 300 °C. Hence, calcination at a higher temperature promoted the growth of MnO_2 NPs located at the external surface of SBA-15 grains.

Redox properties and surface state of 20Mn-MIc-Z samples.

The H_2-TPR profiles are shown in Figure S4. The hydrogen consumption profile obtained for 20Mn-MIc-300 is typical of a MnO_2 phase reduction, being accomplished in two steps. During the first step, the reduction of MnO_2 into Mn_3O_4 takes place (65 % of total H_2 consumption), while during the second step, the reduction of Mn_3O_4 into MnO can be observed (35 % of total H_2 consumption), which is consistent with the theoretical reduction values (67 % and 33 %, respectively). For 20Mn-MIc-500, the proportion area of the first reduction peak is much lower (51 % / 49 %) suggesting the formation of an oxide phase with a lower mean valence (MnO_x with x < 2). This result can be explained by the partial reduction of MnO_2 when increasing the calcination temperature [24, 30]. Based on the H_2-consumption, the Mn average oxidation state (AOS) was calculated, assuming a complete reduction to MnO occurs in the studied temperature range. The Mn AOS calculated for 20Mn-MIc-300 is close to 4, in agreement with the presence of MnO_2 phases identified by XRD analysis. For 20Mn-MIc-500, the Mn AOS is lower (3.6) demonstrating the possible presence of a MnO_x amorphous phases (unidentified by XRD) with lower Mn oxidation state.

The Si 2p XPS spectra (Figure S5) of the 20Mn-MIc-300 and 20Mn-MIc-500 are composed of one main peak at BE ~ 103.8 eV, characteristic of Si^{4+} in SiO_2. For the sample calcined at 300 °C, a smaller Si 2p component at BE ~106.2 eV indicates the presence of Si-OH species [31]. Despite the remaining of Si-OH on the silica surface even after calcination at 500 °C, the ~106.2 eV component is not visible on the Si 2p spectra of 20Mn-MIc-500. In order to estimate the Mn average oxidation state (AOS), the Mn 3s XPS region was analyzed (Figure S6). A correlation between the Mn AOS and the energy difference between the Mn 3s main peak and its satellite (ΔEs) has been proposed by Galakhov *et al.* [32] Equation (1) was used to calculate the Mn AOS (Table 2):

$$\text{Mn AOS} = 8.95 - 1.126 \times \Delta Es \text{ (eV)} \quad (1)$$

The decreases in Mn AOS with calcination temperature increase is confirmed, and values are in agreement with those obtained by H_2-TPR analyses. The O 1s XPS spectra of 20Mn-MIc-300 and 20Mn-MIc-500 are presented in Figure S7. In the O 1s region, two photoelectron peaks can be clearly identified. The O-I component located at ~529.8 eV may be considered as resulting mainly from Mn-O-Mn bonds in MnO_2 [33] while the dominating O-II component at ~532.9 eV is related to O^{2-} species in SiO_2 (Si-O-Si environments).[34] The contribution of the O-I component to the O 1s envelop is ~10 % whatever the calcination temperature. For 20Mn-MIc-300 sample, Mn/Si atomic ratio value is close to the O-II/O-I atomic ratio value, thus confirming the O 1s attribution. However, in comparison with the theoretical ones, Mn/Si atomic ratio value is lower indicating that not all Mn species are detected by XPS analysis.

Table 2. Summary of the XPS results obtained for Mn containing samples.

Sample	B.E. (eV)		ΔEs (eV)	Mn AOS	Mn/Si[1]	O-I/O-II
	O 1s	Si 2p				
20Mn-MIc-300	O-I : 529.4 O-II : 533.0	103.9 106.2	4.36	4.0	0.14 (0.27)	0.10
20Mn-MIc-500	O-I : 529.5 O-II : 532.9	103.6	4.58	3.8	0.16 (0.27)	0.11
5Mn-MIc	O-I : 529.6 O-II : 533.2	103.7	5.12	3.2	0.05 (0.06)	0.03
10Mn-MIc	O-I : 529.4 O-II : 533.3	103.9	4.66	3.7	0.10 (0.12)	0.07
30Mn-MIc	O-I : 529.3 O-II : 533.2	104.0	4.37	4.0	0.16 (0.47)	0.10
20Mn-MIa	O-I : 530.4 O-II : 532.7	103.6	5.93	2.3	0.09 (0.27)	0.04

[1] values in brackets correspond to the expected bulk ratio

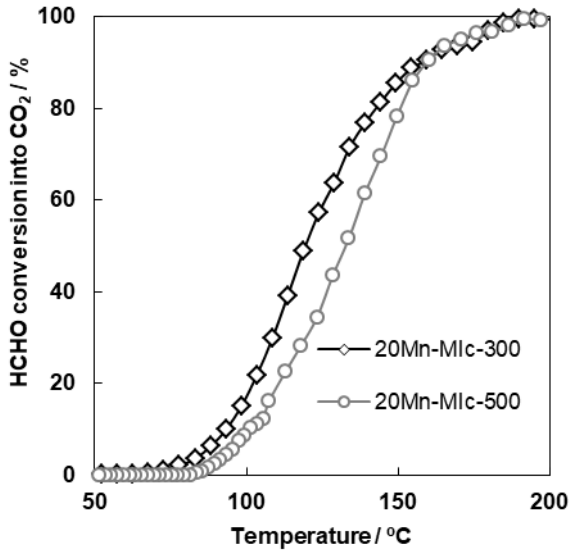

Figure 4. HCHO conversion into CO_2 as a function of the reaction temperature for MnO_x/SBA-15 catalysts (20 wt.% Mn) prepared at different calcination temperatures.

Table 3. Catalytic properties of Mn oxides supported on SBA-15 in formaldehyde total oxidation

Sample	Activity[1] /$mmol_{HCHO\ conv.}$ mol_{Mn}^{-1} h^{-1}	T_{90}[2] (°C)	T_{50}[3] (°C)
20Mn-MIc-300	17.5	160	120
20Mn-MIc-500	10.3	160	133
5Mn-MIc-300	12.4	175	152
10Mn-MIc-300	15.8	168	135
30Mn-MIc-300	13.8	167	114
20Mn-IWI-300	17.5	210	119
20Mn-MIa-300	6.2	176	144

[1] : Measured at 120 °C, [2] : Temperature at 90 % of HCHO conversion into CO_2, [3] : Temperature at 50 % of HCHO conversion into CO_2

Catalytic properties of 20Mn-MIc-Z samples. The catalytic performances of 20Mn-MIc-300 and 20Mn-MIc-500 catalysts were evaluated in the reaction of formaldehyde total oxidation by decreasing the temperature from 200 °C to 50 °C. HCHO was converted into CO_2 and H_2O without any other byproducts. The curves of HCHO conversion into CO_2 as a function of the reaction temperature (light-off curves) are displayed in Figure 4. In the temperature range 75 °C -150 °C, 20Mn-MIc-300 presents the highest activity (Table 3), highlighting the important role of the calcination temperature. The two samples with same MnO_x loading presented similar textural and structural properties but are distinguished by the Mn AOS which decreased with the calcination temperature. Thus, the highest activity can be correlated to the highest Mn AOS. Therefore, for the following studies, a calcination temperature at 300 °C has been kept constant for the preparation of MnO_x-SBA-15 catalysts.

Effect of manganese content

Properties of XMn-MIc-300 (X=5,10,20,30) samples.
The nitrogen adsorption/desorption isotherms at -196 °C as well the pore size distribution of SBA-15 and Mn-MIc samples with different Mn loadings are displayed in Figures S8-S9. The delay in the closure of desorption branches becomes more significant as the Mn content increases, up to 20 wt.%. With Mn loading, the initial pore size distribution of the parent SBA-15 (7.3 nm) is progressively replaced by smaller pore size distribution (~ 5.3 nm). Based on the formation of such second porosity of ~5 nm diameter (Figures S8-S9), previously attributed to MnO_2 NPs occluding partially the silica main mesoporosity, it can be suggested that the optimum for Mn infiltration is 20 wt.%. Besides, specific surface area decreased progressively from 25 % for 5Mn-MIc to 46 % for 20Mn-MIc compared to SSA of SBA-15, while no significant modification in SSA value is observed with a further increase of Mn loading up to 30 wt.% (Figure 5). The pore volume follows the same evolution as the specific surface area.
The XRD patterns are shown in Figure S10. As previously described for 20Mn-MIc sample calcined at 300 °C, whatever the Mn loading, the visible XRD peaks can be whole attributed to a mixture of ε-MnO_2 and β-MnO_2. The average crystallite size values range between ~10 to 12 nm (Table 1), suggesting that MnO_2 is well dispersed even at very high metal loadings.

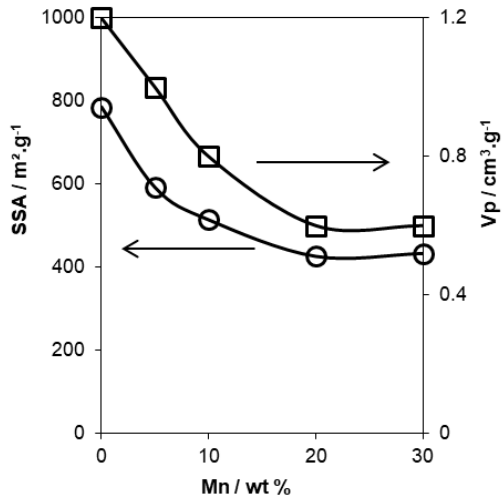

Figure 5. Evolution of the specific surface area and pore volume of MnO_x/SBA-15 materials calcined at 300°C with the Mn loading.

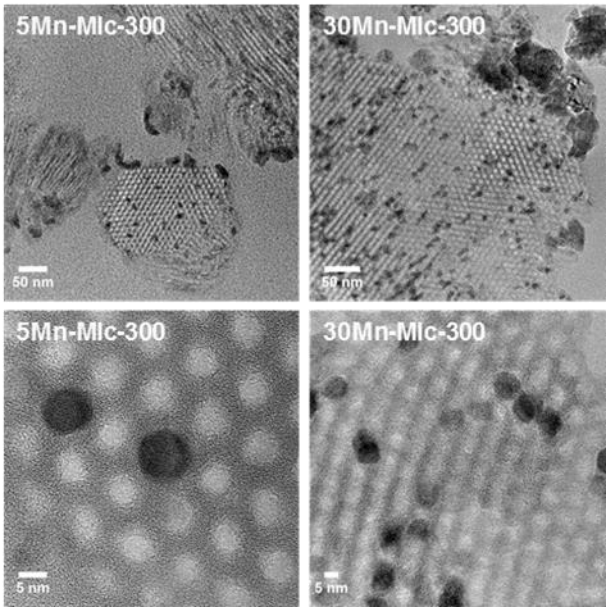

Figure 6. HR-TEM images for MnO_x/SBA-15 materials calcined at 300 °C (5, 30 wt.% Mn).

TEM images for the Mn-loaded materials were collected (Figure 6). The manganese oxide NPs are confined within the mesopores of the SBA-15 for 5Mn-MIc (Figure 6), 20Mn-MIc (Figure 3) and 30Mn-MIc (Figure 6). Even if Mn-containing NPs confined in the main mesopores remain the main phase for all the catalysts, the proportion of external phase is observed to increase with the Mn loading, as observed comparing particle size distributions reported in Figure S11. In addition to the higher proportion of external phases, their size also increase with the MnO_x loading (15 nm, 17 nm and 34 nm for 5, 20 and 30 wt.% Mn, respectively).

When the Mn loading increases, the difference between the average crystal domain size as determined by XRD and the TEM issued average particle size becomes more important. For 30Mn-MIc-300 sample, after calcination at 300°C, formation of aggregates of elementary particles are observed, located at the external surface of the silica grain and inside the silica main mesoporosity. It leads to an average size, observed by TEM, of ~30 nm. XRD however demonstrated the maintaining of an almost constant elementary crystallite size of ~11 nm (Table 1), a value mostly dependent temperature of activation that conditions the crystal growth.

Redox properties and surface state of XMn-MIc-300 samples. The H_2-TPR profiles of XMn-MIc-300 are shown in Figure S12. All the TPR profiles are representative of MnO_2 reduction with 67 % - 33 % distribution between the areas of the two reduction peaks. The reduction occurs as: $MnO_2 \rightarrow Mn_3O_4 \rightarrow MnO$. The Mn AOS is close to 4 for all the samples, in agreement with the presence of MnO_2 phases identified by XRD (Table 2). In the case of 30Mn-MIc-300, a shoulder is observed at higher temperature (T = 435 °C). This could be explained by the presence of larger MnO_2 NPs located at the external surface of the silica grain, which are more difficult to be reduced [25a]. The more important formation of such large – external - NPs for 30Mn-MIc-300 is in agreement with the Mn loading limit, as it has been observed by HR-TEM (Figure 6).

The Si 2p, Mn 3s and O 1s XPS spectra of the XMn-MIc samples are reported in Figures S5, S6 and S7, respectively. The Si 2p spectra are similar regardless of the Mn loading (Si^{4+} from SiO_2). The Mn AOS value, calculated from ΔEs, is lower for 5Mn-MIc-300 sample (3.2) than for samples of higher Mn loadings (3.7-4.0) (Table 2). Considering that H_2-TPR leads to a 4.0±0.1 Mn AOS whatever the loading, the lower surface oxidation state obtained for 5Mn-MIc-300 sample could be related to the smaller MnO_x particle size generated and exclusive localization inside the mesoporosity. As previously proposed, the two peaks in the O 1s region are attributed to O^{2-} species in MnO_x (O-I component) and in SiO_2 (O-II component). The contribution of the O-I component to the O 1s envelope increased with the Mn content up to 20 wt.%, while the Mn/Si atomic ratio values are close to the theoretical ones for 5Mn-MIc-300 and 10Mn-MIc-300, suggesting that the Mn species are homogeneously distributed within the SiO_2 porosity at the lower Mn loadings (Table 2). In contrast, Mn/Si atomic ratio values departs from the theoretical ones for Mn loadings of > 15 wt.% (Table 2), in agreement with the formation of larger MnO_2 particles not entirely detected by XPS and a less homogeneous dispersion in the support porosity.

Catalytic properties of XMn-MIc-300 catalysts

The evolution of the HCHO conversion into CO_2 as a function of the temperature (light-off curve) obtained with the different XMn-MIc-300 catalysts is displayed in Figure 7. By increasing Mn loading, the light-off curves are shifted to lower temperatures. While the T_{90} values are quite similar, the T_{50} is shifted from 152 °C for 5Mn-MIc-300 to 114 °C for 30Mn-MIc-300, respectively (Table 3). The activities (mmole of HCHO converted into CO_2 per hour and per mole of Mn) have been calculated at T = 120 °C in order to evaluate the influence of Mn loading on the catalyst efficiency (Table 3). 120°C was selected considering that, at this temperature, the 5Mn-MIc-300 is active while the other catalysts do not present complete HCHO conversion degree. A maximum of activity is reached for 20Mn-MIc-300 catalyst. This result suggests that the highest MnO_x dispersion is associated to the highest activity in formaldehyde total oxidation (17.5 $mmol_{HCHO\ conv.}$ mol_{Mn}^{-1} h^{-1}). The MnO_2 particles from the external silica grain are larger and exposed less active sites for the formaldehyde oxidation in agreement with the lowest redox properties of such Mn phase (Figure S12). For volatile organic compounds oxidation at low temperature, it is generally accepted a redox mechanism in which the reduction of active species of catalysts (here Mn^{4+}) is the rate determining step while the reoxidation of the active sites occurs in a faster way. Such a mechanism can then explain the parallel between the activity and reducibility obtained in this study.

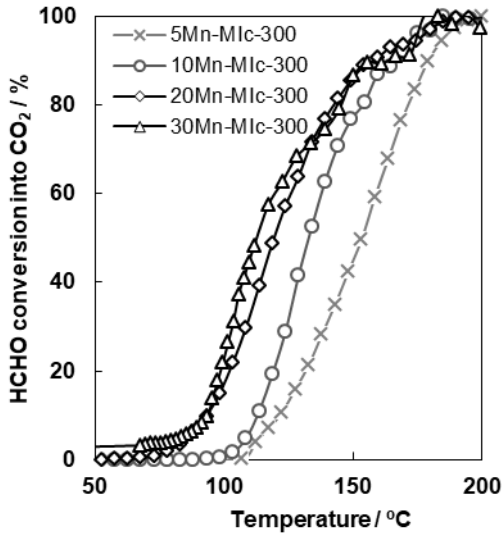

Figure 7. HCHO conversion into CO_2 as a function of the reaction temperature for MnO_x-SBA-15 catalysts with different Mn loadings, calcined at 300 °C.

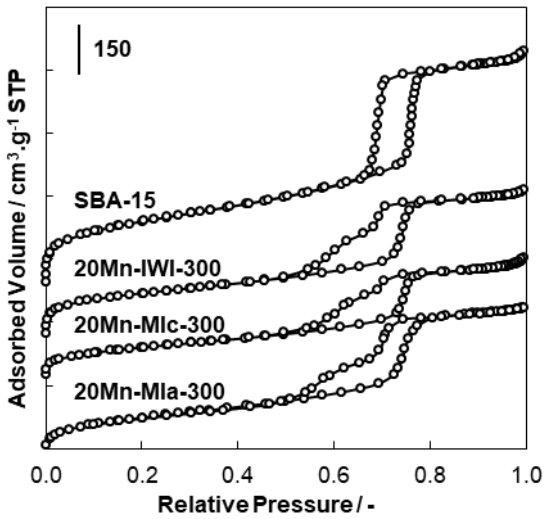

Figure 8. Adsorption/desorption isotherms (vertical shift of 150 $cm^3.g^{-1}$) for MnO_x-SBA-15 samples (20 wt.% Mn) prepared by different synthesis methods.

Effect of synthesis method of the catalyst performances

Properties of 20Mn-YYY-300 (YYY = MIc, MIa, IWI approaches)

The nitrogen adsorption/desorption isotherm of catalysts prepared by different synthesis methods are displayed in Figure 8. No notable change in isotherm shape is observed, and the only difference is on the desorption branch closure and the contribution of the partially occluded porosity. When compared to the MIc and IWI derived materials, the higher pore size (7.3 nm) proportion in the 20Mn-MIa-c300 sample is more important, suggesting that the porosity of SBA-15 is less occluded by the mesopore-confined MnO_x NPs. Besides, SSA decrease is less pronounced for 20Mn-MIa (527 $m^2.g^{-1}$), in comparison with 20Mn-MIc (426 $m^2.g^{-1}$) (Table 1). The low-angle XRD pattern of 20Mn-MIa-300 (Figure S1) confirms, as already concluded for the preparation 20Mn-MIc-300, that the pore network long range ordering is not affected by the preparation steps (presence of three reflections in the 0.8-2.0° 2θ region, Figure S1). Wide-angle XRD patterns of MnO_x-SBA-15 samples (20 wt.% Mn) prepared by different synthesis methods are displayed in Figure 9. No significant differences were observed IWI and MIc samples, both materials presenting mixed ε-MnO_2 and β-MnO_2 phases. On the contrary, the presence of Mn_3O_4 (Hausmannite, JCPDS 80-0382) [35] phase is observed when using melt infiltration on the as-made SBA-15, followed by a calcination at 300 °C (Figure 9). The presence of such mixed Mn^{3+}/Mn^{2+} oxide phase can be explained by the carbon oxidation of P123 during the calcination who can induce the reduction of Mn^{4+} species into Mn^{3+} and Mn^{2+} species. TEM images, and corresponding particles size distributions obtained for the different MnO_x-SBA-15 samples are displayed in Figure 10 and Figure S13. Starting from calcined SBA-15 and using IWI and MIc methods lead to MnO_2 NPs localized inside and outside the mesoporosity even if the external phase remains minor. The size of the external MnO_2 NPs is ~17 nm, while the size of the mesopore confined NPs is fitting with the mesopore size (Figure 10). For the sample prepared by MIa method, infiltration degree within the porosity of the SBA-15 is significantly improved, with only Mn_3O_4 NPs located inside the main mesopores, and a uniform spatial distribution of NPs obtained as well. No external aggregates of Mn_3O_4 can be observed (Figure 10), and approximatively 80% of the particles are of 5-10 nm size (Figure S13). Unexpectedly, a new type of MnO_x NPs formed in an egg-shell shape were generated by MIa when the Pluronic P123 is kept within the porosity for infiltration step. These results demonstrate that infiltration of the molten precursor can be accomplished within the unique nanospaces between the surfactant molecules and the silica walls, as already suggested in recent investigations.[25a,36] Mn_3O_4 NPs appear to cover the walls of SBA-15 mesopores while keeping the mesopores opened. As a consequence, the presence of such new particles together with the unblocked mesoporosity results in improved textural characteristics, as higher surface area and pore volume.[25c]

Redox properties and surface state of 20Mn-YYY-300 samples

H_2-TPR analyses are shown in Figure S14. The Mn AOS values for 20Mn-IWI-300 sample is of ~4, confirming the formation of MnO_2 phases as already observed for 20Mn-MIc-300. Besides, typical MnO_2 reduction profiles with two reduction peaks were observed for these samples. 20Mn-MIa-300 shows a completely different feature. The Mn AOS is of 2.7, far below the values measured for the two other catalysts, but in agreement with the presence of the Mn_3O_4 phase as identified by XRD (Figure S15). XPS analysis confirmed the decrease in Mn AOS on the surface over 20Mn-MIa-300 sample (Table 2). Interestingly, when comparing the O 1s signal of 20Mn-MIc-300 and 20Mn-MIa-300 samples, a shift to higher BE (+1 eV) of the O-I component is observed (Figure S7). This result is in agreement with works of Tang *et al.* which observed the BE decrease of lattice oxygen (O_{latt}) bonding with Mn when Mn valence decreases [37]. Likewise,

it must be pointed out that Mn/Si atomic ratio value substantially departs from the theoretical ones for 20Mn-MIa-300 sample (Table 2) indicating that a significant part of the Mn is not XPS visible which is consistent with a part of Mn phase being located in the core of the silica grain.

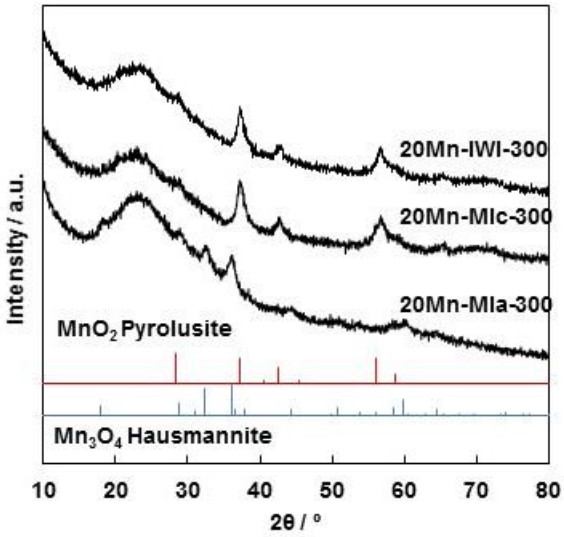

Figure 9. Wide-angle XRD patterns for MnO_x-SBA-15 samples (20 wt.% Mn) prepared by different synthesis methods.

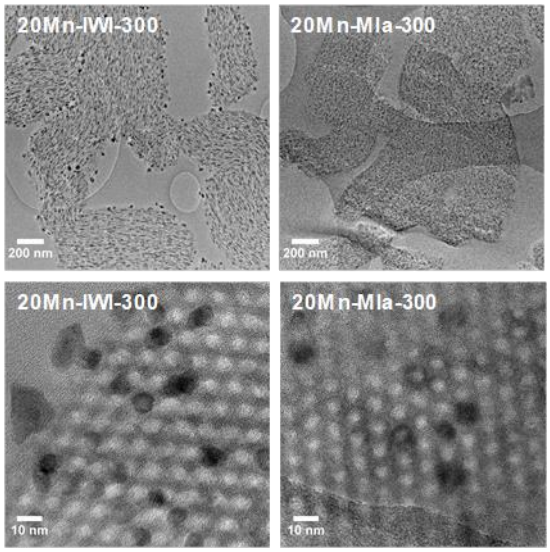

Figure 10. TEM images for MnO_x-SBA-15 samples (20 wt.% Mn) prepared by IWI and MIa methods.

Catalytic properties of 20Mn-YYY-300 catalysts

The HCHO conversion into CO_2 is plotted as a function of reaction temperature (light-off curve) for the MnO_x-SBA-15 catalysts prepared by different procedures (Figure 11). According to the T_{50} values, the following order of performance can be established: 20Mn-MIc-300 ~ 20Mn-IWI-300 > 20Mn-MIc-500 > 20Mn-MIa. The activity is then well correlated with the evolution of the Mn AOS in the different materials, as shown in Figure 12. Therefore, despite the remarkable Mn_3O_4 dispersion and spatial distribution of NPs, 20Mn-MIa-300 catalyst showed a limited catalytic activity due to the low Mn AOS. This result suggests that the Mn^{3+}/Mn^{2+} redox couple is far less efficient than the Mn^{4+}/Mn^{3+} couple in the total formaldehyde oxidation, in agreement with literature on bulk MnO_2 and Mn_3O_4 catalysts for HCHO oxidation.[14, 20a] When compared with the catalysts proposed in the literature, even if the comparison is difficult considering the differences in terms of setup configuration and reaction conditions, these catalysts presents comparable T_{50} (<150°C) than reported for pure – undoped - manganese oxide [8, 14, 24].

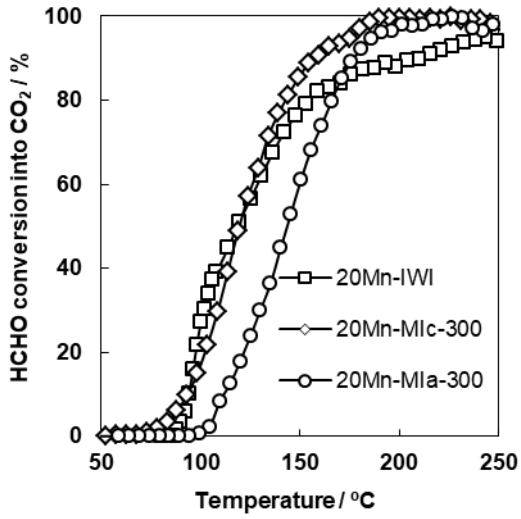

Figure 11. HCHO conversion into CO_2 as a function of the reaction temperature for MnO_x-SBA-15 catalysts (20 wt.% Mn) prepared by different synthesis methods.

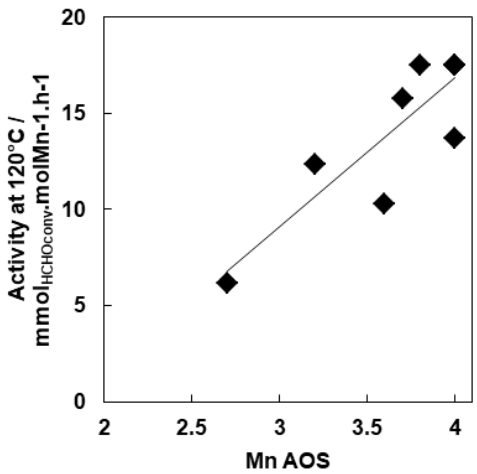

Figure 12. Evolution of the catalyst activity measured at 120 °C as a function of Mn AOS as determined by H_2-TPR.

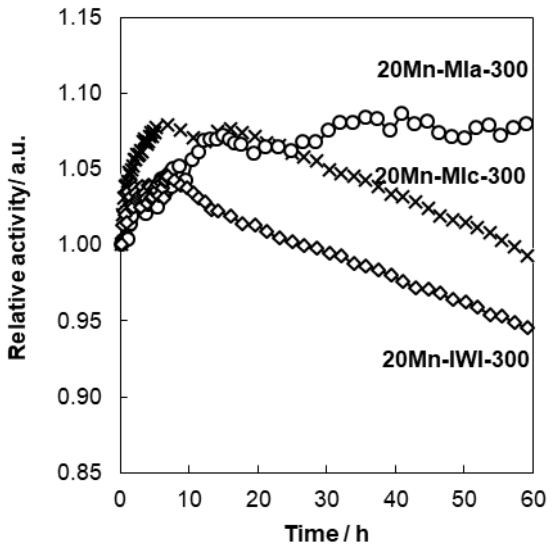

Figure 13. Evolution of the relative activity for MnO_x-SBA-15 catalysts (20 wt.% Mn) prepared by different synthesis methods at a reaction temperature of 170 °C.

Effect of the preparation route on the catalyst stability

Stability tests have been further performed at 170 °C during 60 h and the activity evolution (%conv. divided by initial %conv.) is plotted as a function of time in Figure 13. Moderate deactivation, *i.e.* less than 10%, was measured for 20Mn-IWI and 20Mn-MIc catalysts. However, considering the shape of the curves obtained for the two catalysts, a decrease of the activity is awaited with the increase in reaction time. On the contrary, 20Mn-MIa-300 catalyst shows a remarkable stability. After a short period of activity stabilization, of 15 h, the activity remains stable until the 60 h of reaction. XRD patterns of catalysts after the durability tests (Figure S15) do not allow to detect any evolution when compared to the fresh catalysts: no change in crystalline phase detected; no change in average crystal domain size as measured from X-ray line broadening. The absence of any significant change in crystal domain size is not surprising considering the low reaction temperature applied for the reaction, and the high stability observed for mesopore confined NPs [28]. In addition, H_2-TPR analysis (Figure S16) did not showed any significant modification of the reduction profile in the case of 20Mn-MIc-300. Hydrogen consumed quantification evidenced however a decrease of the Mn AOS from 4.0 (before reaction) to 3.8 after the stability test at 170 °C during 60 h (Figure S16). Similar evolution is measured when studying the Mn AOS on the 20Mn-MIc-300 surface (Mn 3s spectra, Figures S6 and S17), with a slight decrease observed. In the case of 20Mn-MIa-300 catalyst, Mn AOS for the catalyst after test remains at a comparable value (a very small increase being even measured from Mn 3s XPS spectra evolution). Consequently, the progressive decrease in manganese oxidation state is proposed to be at the origin of the catalyst activity decrease (case of MIc and IWI preparation approaches).

In order to test the catalysts under more realistic conditions, stability tests were performed under 50 % relative humidity, at lower temperature (130 °C) (Figure 14). In the presence of water at 130 °C, a limited deactivation is measured over 20Mn-MIc-300 with a loss of only 15 % of its initial activity after 10 h of reaction, and a stable activity reached at the end of the test. Then, the decrease of the reaction temperature added to the presence of water in the reaction feed has a positive effect on the 20Mn-MIc-300 catalyst stability. After reaction under moist atmosphere, the Mn AOS (calculated from TPR experiment, Figure S18) is decreasing to 3.8 after reaction. The limited decrease in activity is obviously related to the slight decrease in Mn AOS but the main difference between dry and humid air reaction is on the obtaining of a stable activity during stability test when water is added to the reaction feed. On the contrary, a significant deactivation is measured with the 20Mn-MIa-300 (45 % in 10h). In agreement with the deactivation observed, the calculated Mn AOS value of 20Mn-MIa after test under moist conditions at 130 °C is of 2.2 (Figure S18). Considering the limited variation of the Mn AOS between before and after test, the observed activity decrease is associated to the water presence. Consequently, the reduced catalyst prepared by the MIa approach is more sensitive to the water presence, while a beneficial effect is observed for the catalyst prepared by MIc procedure.

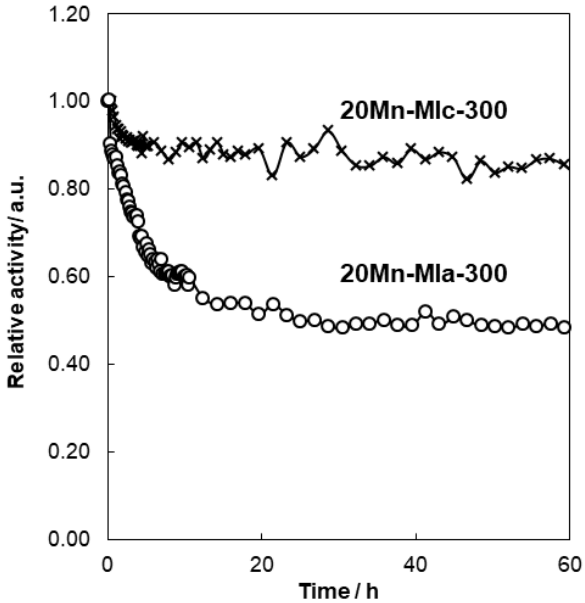

Figure 14. Evolution of the relative activity for MnO_x-SBA-15 catalysts (20 wt.% Mn) prepared by different synthesis methods at a reaction temperature of 130 °C at a R.H. of 50% at 25 °C.

Conclusions

MnO_x NPs confined within the SBA-15 pores were successfully synthesized by melt infiltration. MnO_2 oxide phases have a heterogeneous distribution under the form of both confined and extra-porous nanoparticles, when melt infiltration is applied on calcined support (MIc), the final solids displaying comparable properties than when the catalyst is prepared by incipient wetness impregnation (IWI). A 20 wt.% Mn is an optimal loading to avoid

consequent formation of NPs at the external surface of the SBA-15 silica grains. When the catalyst is prepared by melt infiltration over the support containing the template (MIa), a far better dispersion is obtained (without formation of external phase), in addition to an improved 3D spatial distribution in the support porosity. However, applying the MIa approach leads to the formation of less oxidized Mn_3O_4 phase. Mn AOS was evidenced to directly impact the catalytic activity and is demonstrated the key parameter for obtaining high performances in HCHO catalytic oxidation. Thus, low calcination temperature of 300 °C is preferred for the catalyst activation before reaction. Despite a lower activity due to a decreased Mn AOS (2.3), the MIa catalyst is displaying an excellent stability when reaction is performed at high temperature (170°C) under dry air while the catalyst prepared by MIc suffers from deactivation due to Mn AOS decrease (from 4 to 3.8) upon reaction. However, the MIc catalyst presents better stability at lower temperature (130°C), and when water is added to the reaction feed. Consequently, presence of water and a lower reaction temperature are acting positively for the maintaining of the Mn AOS upon reaction time. An opposite effect of water is observed at low temperature on the Mn_3O_4 phase, and the catalyst prepared by MIa suffers in this case from significant deactivation (45 % in 10h).

Experimental Section

Catalyst synthesis:

The SBA-15 support was synthesized according to the procedure proposed by Zhao et al. [26] 4 g of Pluronic P123 (poly(ethylene oxide)-block-polypropylene oxide)-block-polyethylene oxide)- block, PEO_{20}–PPO_{70}–PEO_{20}, with MW = 5800 g mol^{-1}, BASF Corp) was dissolved in a 1.6 M solution of HCl at 40 °C. 8.5 g of a silica precursor, tetraethyl orthosilicate (TEOS, Sigma-Aldrich), was added dropwise to the solution, and the stirring was maintained for 24 h. The resulting gel was subjected to hydrothermal treatment for 48 h at 100 °C. After recovering by filtration, washing, and drying, the uncalcined SBA-15 is obtained (used for the MIa procedure). SBA-15 is calcined at 550 °C during 6 h (1.5 °C.min^{-1}), in order to obtain the template free support used for MIc and IWI procedures).

Melt infiltration method is applied, starting from $Mn(NO_3)_2$•$4H_2O$ (98%, Sigma-Aldrich) as precursor. The solid precursor was mixed with support (uncalcined SBA-15 - MIa procedure; calcined SBA-15 – MIc procedure). Catalysts are prepared at different Mn loadings (5, 10, 20 and 30 wt%). Procedure adopted involves: (1) the grinding at room temperature for 15 min of precursor and support; (2) a diffusion heat treatment at 38 °C for 12 days; (3) a thermal stabilization by calcination at 300/500°C for 6 h, using a heating rate of 1.5 °C min^{-1}. The samples were labelled XMn-MIc(or MIa)-Z, with X is the Mn loading (5, 10, 20 or 30 wt.%), and Z the calcination temperature applied (300 or 500 °C). Incipient wetness impregnation (IWI) is also used, starting from $Mn(NO_3)_2$•$4H_2O$ (98%, Sigma-Aldrich) as precursor. The appropriate amount of precursor (to obtain 20 wt.% Mn loading) is dissolved in water (volume adjusted to the pore volume of the silica). The aqueous solution of the precursor is mixed with the calcined support, and is dried at 25 °C for 5 days [28]. The solid is then calcined at 300 °C for 6h using a heating rate of 1.5 °C min^{-1} in order to obtain the catalyst denoted 20Mn-IWI.

Catalyst Characterization:

XRD measurements were carried out with a Bruker D5000 vertical goniometer equipped with Cu Kα anticathode (λ=1.5418 Å) and a graphite monochromator. A proportional counter and a 0.04° step size in 2θ were used. The integration time was 2 seconds per step and the scan range was from 10 to 80° in 2θ. The assignment of the various crystalline phases was done by comparison with files in PDF card (Powder Diffraction Files structure data base). The average crystallite sizes (D_{cryst}) of manganese oxides are determined using the X-ray line broadening using the Scherrer equation after Warren's correction for instrumental broadening: $D_{cryst} = 0.89 \cdot \lambda / (\beta / \cos(\theta))$ (D_{cryst} is the mean crystallite size (nm), λ is the X-ray wavelength, β is the line broadening at half the maximum (FWHM) and θ is the Bragg angle). For calculation, the (100) reflection of MnO_2 (2θ = 37.1°) and (211) of Mn_3O_4 (2θ = 36.1°) were used. N_2 adsorption-desorption isotherms were measured at 77K, using a TriStar II 3020 analyzer. Pore volume was determinate at P/P_0 = 0.98. The BET method was used to calculate the specific surface areas, and pore size distribution were calculated using the Barrett-Joyner-Halenda (BJH) model. Before measurements, the samples were heated at 100 °C for 3 hours under vacuum. Elemental analyses were performed by inductively coupled plasma-optic emission spectroscopy 720-ES ICP-OES (Agilent) with axially viewing and simultaneous CCD detection. The sample preparation was made by dissolving 10 mg of dried and ground samples catalyst in 1,5 mL of concentrated nitric acid and 500 µL of hydrofluoric acid solution. Solutions were heated at 50 °C and stirred during 24 hours in a sonication bath to ensure complete dissolution before analysis. Transmission Electronic Microscopy (TEM) was performed on a JEOL 2100 instrument (operated at 200 kV with a LaB_6 source and equipped with a Gatan Ultra scan camera) equipped with Hypernine (Premium) detector (active area: 30mm^2). Before analysis, the samples were embedded in a resin and then sliced using an ultramicrotome (cuts of ~100nm thick). The X-ray photoelectron spectroscopy (XPS) analyses were performed with a Kratos Axis Ultra, equipped with a dual Mg/Al anode. As excitation source was used the monochromatized Al Kα radiation (1486.6 eV). The sample were analysed as pellets, mounted on a double-sided adhesive tape. The pressure in the analysis chamber was in the range of 10^{-9} mbar during data registration. The binding energies of the different core levels were referred to the C1s component set at 284.8 eV. Atomic concentrations were calculated from peak intensity using the sensitivity factors provided with the CasaXPS software (version 2.3.16 PR 1.6). The binding energy values are quoted with a precision of ± 0.15 eV and the atomic percentage with a precision of ± 10%.

Redox properties of the samples were evaluated using a temperature-programmed reduction apparatus form Micromeritics (model AutoChem II). 50 mg of the sample was placed in a quartz reactor and heated under flowing air (50 mL.min^{-1}) at 150 °C for 0.5 h, and then cooled down to room temperature. Then, the reactor was heated from 40 to 1000 °C with a heating rate of 10 °C min^{-1} in a gas mixture (5 vol.% H_2 + 95 vol.% Ar, 50 mL.min^{-1}). The amount of H_2 consumption was assessed using a TCD.

The catalytic oxidation of formaldehyde was performed in a fixed-bed reactor (internal diameter = 10 mm) loaded with the catalyst. Before each test, the catalyst was heated 1 hour at 300 °C under O_2 (20 vol.%) / N_2 flow (100 mL.min^{-1}) to remove water and surface impurities. Gaseous formaldehyde was generated from para-formaldehyde in a permeation tube placed in a permeation chamber (Dynacalibrator, VICI Metronics Inc.). By adjusting the gas carrier flow (O_2 (20 vol.%)/N_2) and the chamber temperature, a stable formaldehyde concentration can be generated. The inlet concentration of formaldehyde was fixed at 100 ppm, and the total flow rate for the reaction was 100 mL.min^{-1}. HCHO tests were performed with 200 mg of catalyst (GHSV = 30000 h^{-1}). The reactor temperature was decreased from 300 °C to 40 °C (0.5 °C.min^{-1}), and the effluent gases were analysed online with a Varian CP-4900 Micro-GC equipped with a TCD and COX type column (1 m). The formaldehyde conversion (X_{HCHO}, %) was

evaluated using the following equation: X_{HCHO} (%) = $[CO_2]$ / $[HCHO]_{ini}$ × 100 (where $[CO_2]$ is the concentration of CO_2 at the temperature T and $[HCHO]_{ini}$ being the initial concentration of formaldehyde determined at the beginning of the test.

Stability tests were performed on the same setup. The temperature were stabilized at the desired temperature (170 °C or 130 °C), and the reaction prolonged during 60 hours. Some experiments are performed under moist air at a relative humidity of 50% at 25 °C.

Acknowledgements

This research is supported by an European Program INTERREG V France—Wallonie—Flanders (FEDER) (DepollutAir). Chevreul institute (FR 2638), Ministère de l'Enseignement Supérieur et de la Recherche and Région Hauts-de-France are also acknowledged for supporting this work. The authors thank Martine Trentesaux, Pardis Simon, Olivier Gardoll and Laurence Burylo for their contribution in XPS, H_2-TPR and XRD measurements.

Keywords: VOC catalytic oxidation ; Formaldehyde ; Manganese oxides ; SBA-15 ; Melt infiltration

[1] A. Mellouki, T.J. Wallington and J. Chen, *Chem. Rev*., **2015**, *115*, 3984-4014.

[2] a) F. Buljubasic and G. Buchbauer, *Flavour Fragr. J*., **2015**, *30*, 5-25. b) X. Tang, Y. Bai, A. Duong, M.T. Smith, L. Li and L. Zhang, *Environ. Int*., **2009**, *35*, 1210–1224. c) T. Salthammer, S. Mentese and R. Marutsky, *Chem. Rev*., **2010**, *110*, 2536-2572.

[3] Y. Sekine*, Atmos. Environ*., **2002**, *36*, 5543-5547.

[4] a) H. Rong, Z. Ryu, J. Zheng, Y. Zhang, *Carbon N. Y*., **2002**, *40*, 2291-2300. b) V. Boonamnuayvitaya, S. Sae-Ung, W. Tanthapanichakoon, *Sep. Purif. Technol*., **2005**, *42*, 159-168.

[5] a) S. Srisuda, B. Virote, *J. Environ. Sci*., **2008**, *20*, 379-384. b) A. Nomura, C. W. Jones, *Chem. - A Eur. J*., **2014**, *20*, 6381-6390.

[6] J.P. Bellat, I. Bezverkhyy, G. Weber, S. Royer, R. Averlant, J. M. Giraudon, J. F. Lamonier, *J. Hazard. Mater.,* **2015**, *300*, 711-717.

[7] a) R. J. Shaughnessy, E. Levetin, J. Blocker and K. L. Sublette, *Indoor Air*, **1994**, *4*, 179-188. b) H. Nakayama, A. Hayashi, T. Eguchi, N. Nakamura, M. Tsuhako, *Solid State Sci*., **2002**, *4*, 1067–1070.

[8] J. Q. Torres, S. Royer, J. P. Bellat, J. M. Giraudon, J. F. Lamonier, *ChemSusChem*, **2013**, *6*, 578–592.

[9] C. L. Nie, Y. Wei, X. Chen, Y. Y. Liu, W. Dui, Y. Liu, M. C. Davies, S. J. B. Tendler, R. G. He, *PLoS One*, **2007**, *2*, 629-643.

[10] a) G. Zhang, Y. Hong, W. He, *Indoor Built Environ*., **2015**, *24*, 138-144. b) Z. J. Wang, Y. Xie, C. J. Liu, *J. Phys. Chem. C*, **2008**, *112*, 19818-19824. c) G. Pang, D. Wang, Y. Zhang, C. Ma, Z. Hao, *Front. Environ. Sci. Eng*., **2016**, *10*, 447-457.

[11] a) L. Wang, H. Yue, Z. Hua, H. Wang, X. Li, L. Li, *Appl. Catal. B Environ.,* **2017**, *219*, 301-313. b) Y. Li, C. Zhang, H. He, *Catal. Today*, **2017**, *281*, 412-417.

[12] a) G. Li, L. Li, *RSC Adv*., **2015**, *5*, 36428-36433. b) Y. Wang, C. Dai, B. Chen, Y. Wang, C. Shi, X. Guo, *Catal. Today*, **2015**, *258*, 616-626.

[13] X. Liu, J. Lu, K. Qian, W. Huanf, M. Luo, *J. Rare Earths*, **2009**, *27*, 418–424.

[14] J.Q. Torres, J. M. Giraudon, J.-F. Lamonier, *Catal. Today*, **2011**, *176*, 277-280.

[15] Y. Huang, H.Li, M. S. Balogun, H. Yang, Y. Tong, X. Lu, H. Ji, *RSC Adv.,* **2014**, *5*, 7729-7733.

[16] B. Bai, H. Arandiyan, J. Li, *Appl. Catal. B Environ*., **2013**, *142-143*, 677-683.

[17] D. W. Kwon, P. W. Seo, G. J. Kim and S. C. Hong, *Appl. Catal. B Environ*., **2015**, *163*, 436-443.

[18] a) L. Zhou, J. Zhang, J. He, Y. Hu,H. Tian, *Mater. Res. Bull*., **2011**, *46*, 1714-1722. b) J. Zhang, Y. Li, L. Wang, C. Zhang, H. He, *Catal. Sci. Technol.,* **2015**, *5*, 2305-2313.

[19] H. Chen, J. He, C. Zhang, H. He, *J. Phys. Chem. C*, **2007**, *111*, 18033-18038.

[20] a) H. Tian, J. He, L. Liu, D. Wang, Z. Hao, C. Ma, *Microporous Mesoporous Mater*., **2012**, *151*, 397-402. b) T. Chen, H. Dou, X. Li, X. Tang, J. Li, J. Hao, *Microporous Mesoporous Mater.,* **2009**, *122*, 270-274.

[21] L. Zhou, J. He, J. Zhang, Z. He, Y. Hu, C. Zhang, H. He, *J. Phys.Chem.C*, **2011**, 115, 16873–16878.

[22] J. Li, P. Zhang, J. Wang, M. Wang, *J. Phys.Chem.C*, **2016**, 120, 24121–24129.

[23] L. Lu, H. Tian, J. He, Q. Yang, *J. Phys.Chem.C*, **2016**, 120, 23660–23668.

[24] R. Averlant, S. Royer, J. M. Giraudon, J. P. Bellat, I. Bezverkhyy, G. Weber, J. F. Lamonier, *ChemCatChem*, **2014**, *6*, 152-161.

[25] a) P. E. De Jongh, T. M. Eggenhuisen, *Adv. Mater.,* **2013**, *25*, 6672-6690. b) W.H. Tian, L.B. Sun, X.L. Song, X.Q. Liu, Y. Yin, G.S. He, *Langmuir*, **2010**, *26*, 17398-17404. c) C. Ciotonea, B. Dragoi, A. Ungureanu, C. Catrinescu, S. Petit, H. Alamdari, E. Marceau, E. Dumitriu, S. Royer, Catal. Sci. Technol., **2017**, 7, 5448-5456. d) T.M. Eggenhuisen, J.P. Den Breejen, D. Verdoes, P.E. De Jongh, K.P. De Jong, *J. am. Chem. Soc*, **2010**, *132*, 18318-18325. e) S.Chen, C. Ciotonea, A. Ungureanu, E. Dumitriu, C. Catrinescu, R. Wojcieszak, F. Dumeignil, S. Royer, Catal. Today, **2019**, *334*, 48-58.

[26] D. Zhao, J. Feng, N. Huo, G. Melosh, H. Fredrickson, B. F. Chmelka, G. D. Stucky,, *Science*, **1998**, *279*, 548–552.

[27] J.R.A. Sietsma, J.D. Meeldijk, M. Versluijs-Helder, A. Broersma, A. Jos Van Dillen, P.E. De Jongh and K.P. De Jong, *Chem. Mater*., **2008**, *20*, 2921-2931.

[28] A. Ungureanu, B. Dragoi, A. Chirieac, C. Ciotonea, S. Royer, D. Duprez, A. S. Mamede, E. Dumitriu, *ACS Appl. Mater. Interfaces*, **2013**, *5*, 3010-3025.

[29] B. Bai, Q. Qiao, J.Li, J. Hao, *Chinese J. Catal*., 2016, *37*, 27-31.

[30] L.S. Dent Glasser, I. B. Smith, *Mineral. Mag. J. Mineral. Soc*., **1968**, *36*, 976-987.

[31] E. Paparazzo, *Appl. Surf. Sci*., **1993**, *72*, 313-319.

[32] V.R. Galakhov, M. Demeter, S. Bartkowski, M. Neumann, N.A. Ovechkina, E.Z. Kurmaev, N.I. Lobachevskaya, Y.M. Mukovskii, J. Mitchell and D.L. Ederer, Phys. Rev. B - *Condens. Matter Mater. Phys*., **2002**, *65*, 1-4.

[33] a) A.K. Sinha, K. Suzuki, M. Takahara, H. Azuma, T. Nonaka, N. Suzuki, N. Takahashi, *J. Phys. Chem. C*, **2008**, *112*, 16028-16035. b) L. Zhu, J. Wang, S. Rong, H. Wang, P. Zhang, *Appl. Catal. B Environ.*, **2017**, *211*, 212-221.

[34] a) E. Paparazzo, M. Fanfoni, E. Severini, *Appl. Surf. Sci*., **1992**, *56-58*, 866-872. b) R. Castillo, B. Koch, P. Ruiz, B. Delmon, *J. Catal*., **1996**, *161*, 524-529.

[35] Y.F. Han, F. Chen, K. Ramesh, Z. Zhong, E. Widjaja, L. Chen, *Appl. Catal. B Environ*., **2007**, *76*, 227-234.

[36] C. Ciotonea, I. Mazilu, B. Dragoi, C. Catrinescu, E. Dumitriu, A. Ungureanu, H. Alamdari, S. Petit, S. Royer, *ChemNanoMat*, **2017**, *3*, 233-237.

[37] Q. Tang, L. Jiang, J. Liu, S. Wang, G. Sun, *ACS Catal*, **2014**, *4*, 457-463.

Entry for the Table of Contents (Please choose one layout)

Layout 1:

FULL PAPER

Conventional and optimized melt infiltration were used to prepare MnO_x nanoparticles encapsulated within the silica pores for the catalytic oxidation of formaldehyde

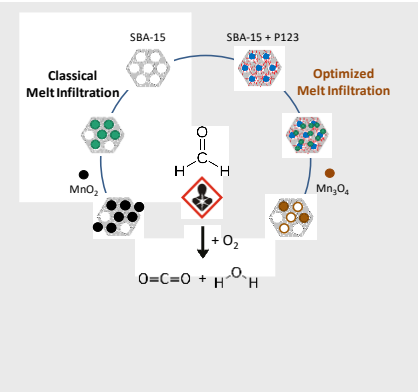

Guillaume Rochard,[a] Carmen Ciotonea,[a] Adrian Ungureanu,[b] Jean-Marc Giraudon,[a] Sébastien Royer,[a] Jean-François Lamonier*[a]*

Page No. – Page No.

MnO_x loaded mesoporous silica for the catalytic oxidation of formaldehyde. Effect of the melt infiltration conditions on the activity – stability behavior

Layout 2:

FULL PAPER

((Insert TOC Graphic here; max. width: 11.5 cm; max. height: 2.5 cm))

*Author(s), Corresponding Author(s)**

Page No. – Page No.

Title

Text for Table of Contents